*Article*

# A Theoretical Model for the Hydraulic Permeability of Clayey Sediments Considering the Impact of Pore Fluid Chemistry

**Lixue Cao** [1,2,3], **Hang Zhao** [1,2,3], **Baokai Yang** [1,2,3], **Jian Zhang** [1,2,3], **Hongzhi Song** [1,2,3], **Xiaomin Fu** [1,2,3] **and Lele Liu** [4,*]

1   Qingdao Key Laboratory of Groundwater Resources Protection and Rehabilitation, Qingdao 266101, China
2   Key Laboratory of Geological Safety of Coastal Urban Underground Space, Qingdao 266101, China
3   Qingdao Geo-Engineering Surveying Institute (Qingdao Geological Exploration Development Bureau), Qingdao 266101, China
4   Shandong Engineering Research Center of Marine Exploration and Conservation, Ocean University of China, Qingdao 266100, China
*   Correspondence: lele.liu@ouc.edu.cn

**Abstract:** The chemistry of the pore fluid within clayey sediments frequently changes in various processes. However, the impacts of pore fluid chemistry have not been well included in the hydraulic permeability model, and the physical bases behind the salinity sensitivity of the hydraulic permeability remains elusive. In this study, a theoretical model for the hydraulic permeability of clayey sediments is proposed, and impacts of the pore fluid chemistry are quantitatively considered by introducing electrokinetic flow theory. Available experimental data were used to verify the theoretical model, and the verified model was further applied as a sensitivity analysis tool to explore more deeply how hydraulic permeability depends on pore fluid chemistry under different conditions. Coupling effects of pore water desalination and the effective stress enhancement on the hydraulic permeability of marine sediments surrounding a depressurization wellbore during hydrate production are discussed. Results and discussion show that the hydraulic permeability reduction is significant only when the electric double layer thickness is comparable to the characteristic pore size, and the reduction becomes more obvious when the ion mobility of the saline solution is smaller and the surface dielectric potential of clay minerals is lower. During gas hydrate production in the ocean, the salinity sensitivity of the hydraulic permeability could become either stronger and weaker, depending on whether the original characteristic pore size of marine sediments is relatively large or small.

**Keywords:** seawater intrusion; gas hydrate; salinity; electro-viscous effect; electric double layer; pore size

## 1. Introduction

Clay minerals are hydrous silicates with layered structures, and layer silicates are essentially composed of silicon–oxygen tetrahedral and aluminum-bearing octahedral units which are stacked in a regular array as continuous two-dimensional sheets [1]. These distinctive structures largely determine the unique properties (e.g., swelling behavior, high cation exchange capacity, large specific surface area, etc.) of clay minerals, and the presence of clay minerals in soils could dramatically alter their chemical and physical properties [2,3]. Soil parent materials on the continent turn into clay minerals when subjected to weathering and erosion processes, and the clay minerals are carried by rivers, wind or ice into the sea [4]. On the seafloor, clay minerals continuously deposit, and the deposited clay minerals could be further transported to the ocean floor by gravitational flows (e.g., turbidity currents and debris flows) [5]. This results in an extremely wide distribution of clay minerals in marine sediments globally [5,6].

The pore fluid chemistry of clayey sediments frequently changes during various processes [7]. Clayey and silty sediments along the continental margins host more than 90% of global gas hydrate accumulation [8,9], and methane recovery from gas hydrates could reduce the pore fluid salinity, as one volume of gas hydrate would dissociate to about 0.8 volumes of freshwater [10]. Fresh groundwater salinization widely occurs in offshore and coastal regions due to seawater intrusion [11,12], and seawater–freshwater mixing zones would move landward if coastal aquifers were further overexploited or sea levels continuously increased [13,14]. Changes in pore fluid chemistry could alter the mechanical and hydraulic properties of clays or clayey sediments [7,15–20], and hydraulic permeability decreases dramatically when subjected to pore fluid desalination [21–24]. Accounting for the hydraulic permeability responses to changing salinities of pore fluid within clayey sediments is important for assessing the mechanical instability and production efficiency of methane extraction from gas hydrates, as well as for evaluating available freshwater storage volume and contamination of production wells under the threat of seawater intrusion. This is mainly because the hydraulic permeability of marine sediments is a major factor in controlling the multiple physical coupling processes of hydrate production [25–27] and seawater intrusion [28–30].

To numerically simulate the multiple physical coupling processes, theoretical or empirical models of hydraulic permeability are basically required and, in developments of the models, the interconnected pores within soils are frequently represented by using a bundle of capillary tubes [31,32]. In these capillary tubes, the fluid moves in parallel layers without disrupting or mixing (i.e., laminar fluid flow), and the flow rate of each capillary tube can be calculated by using the Hagen–Poiseuille equation [33]. Once the total flow rate of all the capillary tubes has been determined, Darcy's law [34,35] is adopted to calculate the hydraulic permeability of soils. In these hydraulic models, the Kozeny–Carman (KC) equation [36,37] is the most widely accepted and highly applicable model. The KC equation is roughly valid for sandy and silty soils but not for clayey soils [38]. The surface of clay particles in nature is negatively charged, and pore fluid (i.e., water molecules) near the clay particle surface is intensively constrained by electric field forces [39]. The constrained pore fluid and the pore fluid in unconnected pores make little contribution to the pore fluid transportation. For this reason, the porosity in the KC equation is modified as the effective porosity within clayey soils, in order to improve model usability [40]. The KC equation could also be modified by replacing the specific surface area with soil indexes, such as liquid limit [41], soil water characteristic curve [42], and cation exchange capacity [43]. As an alternative to the KC equation family, exponential models of hydraulic permeability have been proposed for clayey soils based on vast flushing data [44–46]. However, due to the empirical or semiempirical nature of these models for clayey soils, the impact of pore fluid chemistry has not been well addressed.

Clayey sediments inherently imply small pore sizes [47], and the equivalent pore diameter ranges from several hundred microns down to approximately several nanometers [48,49]. When a polar liquid (e.g., seawater) is forced through microchannels (e.g., small pores within clays) under an externally applied pressure gradient, an electrostatic potential (i.e., the streaming potential) is generated along the direction opposite to the pressure-driven flow due to the presence of an electrical double layer (EDL) near the solid–liquid interface [50,51]. The EDL is generally divided into two regions, a compact layer (also called the Stern or Helmholtz layer) and a diffuse layer (also called the Guoy–Chapman layer). Water molecules in the diffuse layer are pulled by ions moving under the induced streaming potential and a secondary liquid flow opposite to the pressure-driven flow occurs, resulting in an overall reduced flow rate in the external pressure gradient direction [52,53]. This retardation effect is usually referred to as the electro-viscous effect [54], and this electro-viscous effect becomes stronger when the characteristic dimensions of small pores and the EDL thickness become closer to each other [55]. The electro-viscous effect is treated as a factor inducing a non-flowing boundary layer coating capillary tubes (i.e., to shrink the tubes for fluid flow), and the behavior of fluid flow through low-permeability porous media

(e.g., clays) is analytically explored [56]. To the best of our knowledge, the electro-viscous effect has not been well included in developments of the hydraulic permeability model for clayey soils, and impacts of the pore fluid chemistry on hydraulic permeability have not been sufficiently explored.

This study proposes a theoretical model for the hydraulic permeability of clayey sediments, and impacts of the pore fluid chemistry are quantified by introducing the electrokinetic flow theory. The proposed theoretical model is firstly verified by experimental data, and sensitivity analyses are performed to explore how the hydraulic permeability alters with changing pore fluid salinity under different pore sizes, ion mobilities, and clayey minerals. Results are further extended by considering the consolidation behavior of clayey sediments, and insight is finally provided into the hydraulic permeability change when subjected to combined variations of pore fluid chemistry and external stress.

## 2. Model Development

The pore structure of clayey sediments is inherently complex, and the range of pore sizes can cover almost five orders of magnitude [48]. To simplify the problem and focus on the impact of pore fluid chemistry, the pore space within clayey sediments is represented by a bundle of tortuous capillary tubes, and the radii of all the capillary tubes are the same, which denotes the characteristic pore size. Inside, the walls of all the capillary tubes are uniformly and negatively charged to a potential $\zeta$ (i.e., the zeta potential) relative to the bulk saline solution filling the tubes, and an EDL with a thickness of $\kappa^{-1}$ is developed near the inside wall (Figure 1). The thickness is temperature dependent [57], and the symbol $\kappa$ represents the Debye–Hückel parameter [58], which could be calculated as

$$\kappa = \left( \frac{8\pi n_0 e_0{}^2}{\varepsilon_0 \epsilon k T} \right)^{\frac{1}{2}} \tag{1}$$

where $n_0$ stands for the bulk number concentration of ions in the saline solution (i.e., electrolyte concentration, ions·m$^{-3}$), $e_0$ for the proton charge (C), $\varepsilon_0$ for the vacuum permittivity (F·m$^{-1}$), $\epsilon$ for the dielectric constant of saline solution, $k$ for the Boltzmann's constant, and $T$ for the absolute temperature (K). The bulk number for concentration of ions is given by

$$n_0 = \frac{c_0 N_A}{M_s} \tag{2}$$

where $N_A$ stands for the Avogadro constant, $c_0$ for the mass concentration (i.e., the salinity), and $M_s$ for the molar mass of solute (i.e., sodium chloride in this study) in the saline solution (kg·mol$^{-1}$).
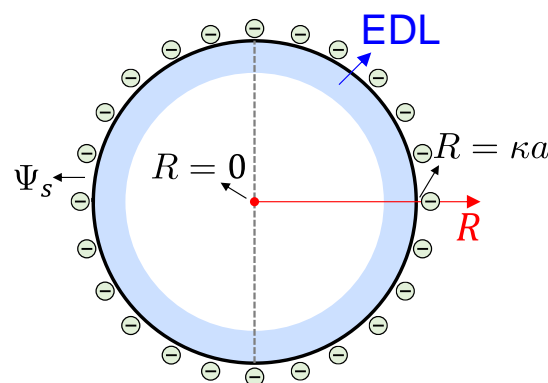


**Figure 1.** Illustration of a capillary tube with an electrical double layer (EDL) developed near the inside wall, which is uniformly and negatively charged to a dimensionless potential $\Psi_s$. Thickness of the EDL is expressed as $\kappa^{-1}$, and the capillary tube radius is demonstrated as $a$. A dimensionless radial coordinate $R$ is set, starting at the center of the capillary tube.

For each capillary tube, the volumetric flow rate $q$ is given by [54]

$$q = \frac{\pi a^4}{8\mu}\frac{\Delta P}{L_t} - \frac{\varepsilon_0^2 \epsilon^2 \zeta^2 a^2 (1-G)F}{16\pi\lambda\mu^2}\frac{\Delta P}{L_t} \tag{3}$$

where $a$ stands for the capillary tube radius (m), $\mu$ for the saline solution viscosity (Pa·s), $L_t$ for the capillary tube length (m), $\frac{\Delta P}{L_t}$ for the external pressure gradient (Pa·m$^{-1}$), and $\lambda$ for the saline solution conductivity (S·m$^{-1}$), and this could be calculated as

$$\lambda = 2me_0 n_0 \tag{4}$$

where $m$ stands for the ion mobility (m$^2$·s$^{-1}$·V$^{-1}$). The symbol $G$ in Equation (3) represents an integral function, which is given by [54]

$$G = \frac{2}{(\kappa a)^2 \Psi_s}\int_0^{\kappa a} R\Psi(R)dR \tag{5}$$

where $R$ stands for the dimensionless radial coordinate, and $R = \kappa r$ with the symbol $r$ denoting the radial coordinate; $\Psi(R)$ represents the dimensionless potential due to the negatively charged inside wall; and $\Psi_s = \Psi(\kappa a) = \frac{e_0 \zeta}{kT}$ denotes the dimensionless zeta potential. The symbol $F$ in Equation (3) represents another integral function, which is given by [54]

$$F = \frac{\frac{1}{2}(\kappa a)^2(1-G)}{\int_0^{\kappa a} R\cosh\Psi(R)dR + \beta^* \int_0^{\kappa a} R\left(\frac{d\Psi(R)}{dR}\right)^2 dR} \tag{6}$$

where $\beta^*$ represents a dimensionless parameter, which is defined as [54]

$$\beta^* = \frac{\varepsilon_0^2 \epsilon^2 k^2 T^2 \kappa^2}{16\pi^2 \mu\lambda e_0^2} \tag{7}$$

The dimensionless potential $\Psi(R)$ is governed by the Poisson–Boltzmann equation [59], which is widely used to depict the ion distribution around a charged surface, and a dimensionless form of the Poisson–Boltzmann equation is given by [54]

$$\frac{1}{R}\frac{d}{dR}\left(R\frac{d\Psi(R)}{dR}\right) = \sinh\Psi(R) \tag{8}$$

The boundary conditions for a capillary tube with a negatively charged inside wall are

$$\Psi(R = \kappa a) = \Psi_s = \frac{e_0 \zeta}{kT} \tag{9}$$

and

$$\left.\frac{d\Psi(R)}{dR}\right|_{R=0} = 0 \tag{10}$$

There is not a single simple analytical solution available for Equations (8)–(10), unless mathematical approximations are adopted [54,60]. In this study, mathematical approximations are not used, and Equations (8)–(10) are numerically solved by using an iteration method. Prior to iterative computations, the hyperbolic sine function $\sinh\Psi(R)$ is written as a truncated series, and Equation (8) turns into

$$\frac{1}{R}\frac{d}{dR}\left(R\frac{d\Psi(R)}{dR}\right) = \Psi(R) + \frac{\Psi(R)^3}{3!} + \frac{\Psi(R)^5}{5!} + \frac{\Psi(R)^7}{7!} + \frac{\Psi(R)^9}{9!} \tag{11}$$

Once the volumetric flow rate $q$ is determined, the total volumetric flow rate $Q$ of the capillary tube bundle could be calculated as

$$Q = \frac{A\phi}{\pi a^2} q \tag{12}$$

where $A$ stands for the cross-sectional area (m$^2$) of the representative volume element (REV) of clayey sediments, and $\phi$ for the porosity of clayey sediments. According to Darcy's law [34,35], the hydraulic permeability $K$ of clayey sediments is given by

$$K = \frac{\mu Q}{A \frac{\Delta P}{L}} \tag{13}$$

where $L$ denotes the REV side length (m) along the porous flow direction, and $L = \frac{L_t}{\tau}$, where $\tau$ represents the hydraulic tortuosity.

To reexamine the polynomial on the right-hand side of Equation (3), the first term is exactly consistent with the Hagen–Poiseuille equation, and the second term is solely as a result of the electrokinetic phenomena. The reduced volumetric flow rate resembles the volumetric flow rate of a fluid with an increased viscosity (i.e., the electro-viscous effect), and an apparent viscosity $\mu_a$ is used to recalculate the volumetric flow rate as

$$q = \frac{\pi a^4}{8\mu_a} \frac{\Delta P}{L_t} \tag{14}$$

By comparison of Equations (3) and (14), the apparent viscosity $\mu_a$ is given by

$$\frac{\mu_a}{\mu} = \left(1 - \frac{8\beta^* \Psi_s^2 (1-G)F}{(\kappa a)^2}\right)^{-1} \tag{15}$$

Equation (11) and the boundary conditions (Equations (9) and (10)) are firstly dispersed by using the finite difference method, and the iterative computations use the following equation

$$\begin{aligned}
&\left(1 - \frac{1}{2(i-1)}\right)\Psi_{i-1} - (2 + \Delta R \Delta R)\Psi_i + \left(1 + \frac{1}{2(i-1)}\right)\Psi_{i+1} \\
&= (\Delta R \Delta R)\left(\frac{\Psi_i^3}{3!} + \frac{\Psi_i^5}{5!} + \frac{\Psi_i^7}{7!} + \frac{\Psi_i^9}{9!}\right)
\end{aligned} \tag{16}$$

where $\Delta R$ stands for the spatial step, $i$ for the node number, and $\Psi_N = \Psi_s$ while $\Psi_1 = \Psi_2$ according to Equations (9) and (10). Then, the symbols $G$ and $F$ could be calculated according to Equations (5) and (6), followed by computation of the apparent viscosity $\mu_a$ according to Equation (15). Finally, the hydraulic permeability $K$ could be calculated according to Equation (13). All the computations in this study are accomplished by using a self-developed code based on the programming platform of MATLAB R2016a.

## 3. Model Verification

Numerical computations are conducted with different total grid numbers to study the grid dependency, and values of the model parameter are summarized in Table 1. Calculated results for the dimensionless dielectric potential $\Psi$, the dimensionless parameters $G$ and $F$, and the normalized viscosity $\Gamma = \frac{\mu_a}{\mu}$ are shown in Figure 2. It is obvious that, when the total grid number is larger than 100, the dimensionless dielectric potential curves overlap each other (Figure 2a), and values of $G$, $F$, and $\Gamma$ are fully independent of the total grid number. In this study, a total grid number of 10,001 is applied to the following computations.

**Table 1.** Values of the model parameters.

| Parameters | Values | References |
|---|---|---|
| Proton charge, $e_0$ (C) | $1.6028 \times 10^{-19}$ | [61] |
| Dielectric constant of saline solution, $\epsilon$ (dimensionless) | 80 | [54] |
| Avogadro constant, $N_A$ (dimensionless) | $6.0221 \times 10^{23}$ | [62] |
| Boltzmann's constant, $k$ (J·K$^{-1}$) | $1.38065 \times 10^{-23}$ | [61] |
| Ion mobility, $m$ (m$^2$·s$^{-1}$·V$^{-1}$) | $5.19 \times 10^{-8}$ | [63] |
| Surface dielectric potential, $\zeta$ (V) | $-49.3 \times 10^{-3}$ | [39] |
| Viscosity, $\mu$ (Pa·s) | $1.0 \times 10^{-3}$ | [54] |
| Mass concentration of sodium chloride, $c_0$ (dimensionless) | $3.5 \times 10^{-2}$ | [64] |
| Hydraulic tortuosity, $\tau$ (dimensionless) | 1.15 | [65] |
| Molar mass of sodium chloride, $M_s$ (kg·mol$^{-1}$) | $58.5 \times 10^{-3}$ | |
| Capillary tube radius, $a$ (m) | $1.0 \times 10^{-8}$ | |
| Temperature, $T$ (K) | 293 | |
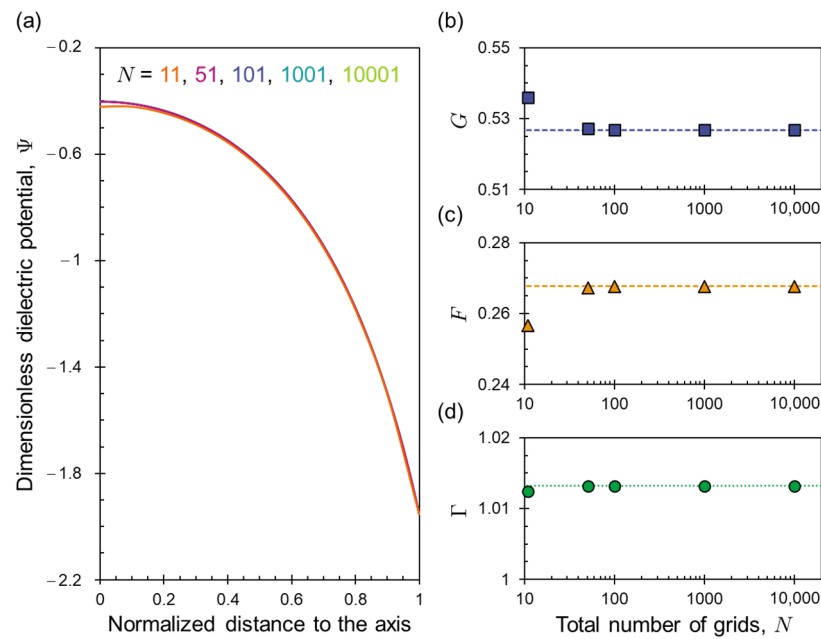


**Figure 2.** Results of the dimensionless dielectric potential $\Psi$ (**a**), the dimensionless parameters $G$ (**b**) and $F$ (**c**), and the normalized viscosity $\Gamma$ (**d**) under different conditions of the total grid number $N$.

Mesri and Olson [45] prepared slurries of kaolinite, illite, and smectite (mainly montmorillonite) in water by repeatedly washing with concentrated saline solutions. The slurries were first consolidated to pressures ranging from 4.309 kPa to 5.985 kPa in a special sedimentation tube and then further consolidated to a pressure of 3.064 MPa through eight steps in a consolidation ring with a diameter of 63.5 mm. When subjected to consolidation pressure changes, the measured settlement data are used to extract the coefficient of permeability. Coefficients of permeability of all three clay minerals in saline solutions with different salinities were reported, and these experimental results are used to verify the model proposed in this study. The coefficient of permeability $K^*$ (i.e., the hydraulic conductivity, m·s$^{-1}$) is transformed into the hydraulic permeability $K$ (m$^2$) by $K = \frac{\mu}{\rho g} K^*$, where $\rho$ is the fluid density and $g$ is the gravitational acceleration. The void ratio $e_v$ of clay minerals was measured and used to calculate the porosity $\phi = \frac{e_v}{1+e_v}$. The surface potential of kaolinite, illite, and montmorillonite minerals is $-0.0538 \times 10^{-3}$ V, $-49.3 \times 10^{-3}$ V, and $-19.3 \times 10^{-3}$ V, respectively [39]. The hydraulic tortuosity and the characteristic pore size of clay minerals were unfortunately not measured, a common value of 1.15 was set for the hydraulic tortuosity (Table 1), and the characteristic pore size was acquired by fitting the hydraulic permeability.
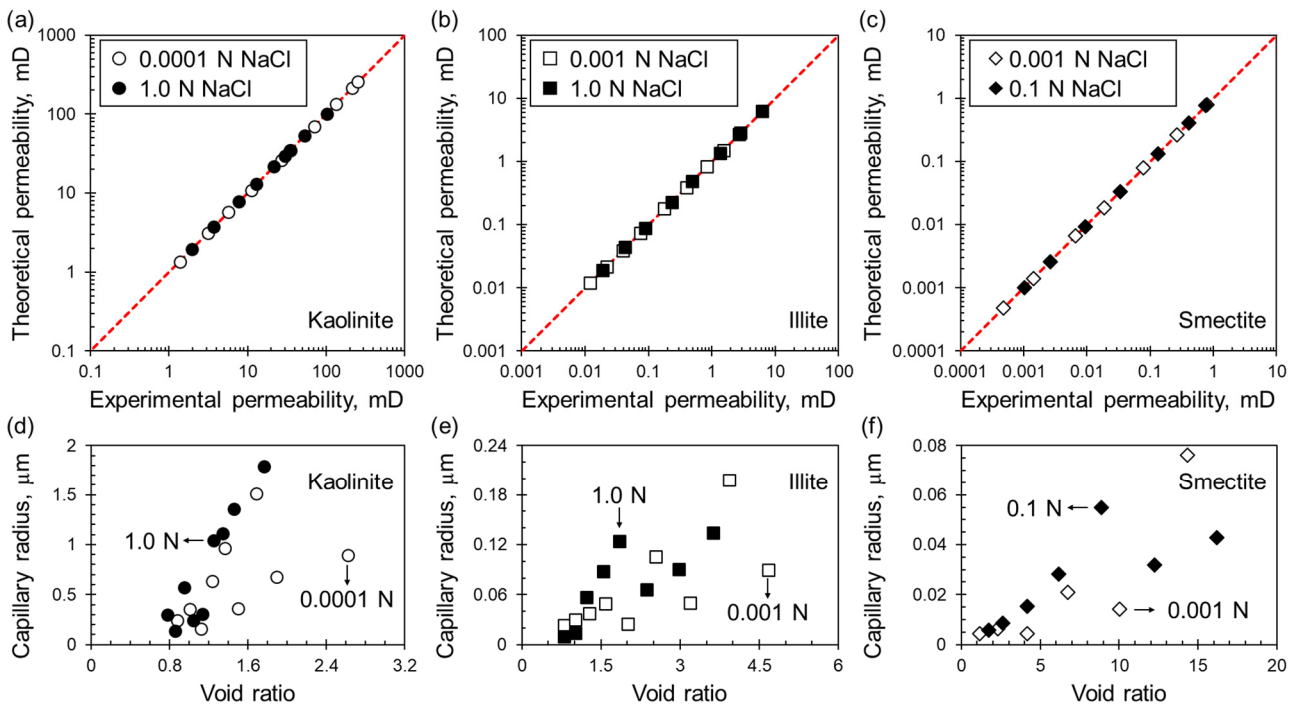
Experimental and theoretical permeabilities are compared in Figure 3, and the fitted capillary radius is also included. It is obvious that the theoretical permeability is very

consistent with the experimental permeability for all three clay minerals under different conditions of sodium chloride concentration, and values of the Lin's Concordance Correlation Coefficient (LCCC) [66,67] are all larger than 0.999 (Table 2). The fitted capillary radius (i.e., the characteristic pore size) generally ranges from 0.1 μm to 1.8 μm for kaolinite (Figure 3d), from 0.01 μm to 0.20 μm for illite (Figure 3e), and from 0.005 μm to 0.08 μm for smectite (Figure 3f). These values of the characteristic pore size are quite comparable with published data [48,49,68,69]. For example, the characteristic pore size of three clayey soils located in China generally ranges from 0.004 μm to 0.01 μm [68], the pore size of compacted Edgar Plastic kaolinite mostly ranges from 0.03 μm to 3.0 μm, the characteristic pore size of Macon kaolinite is roughly 0.2 μm, and the characteristic pore size of Fithian illite is roughly 0.1 μm [48]; The characteristic pore size of natural clays is about 0.2 μm [49], the characteristic pore size of Wyoming montmorillonite is 0.07 μm, and the characteristic pore size of Georgia kaolinite is roughly 0.15 μm [69]. In addition, the fitted capillary radius generally decreases with decreasing void ratio due to consolidation, and the overall trend is consistent with the theoretical analyses [70,71], which offer an equation depicting the trend as

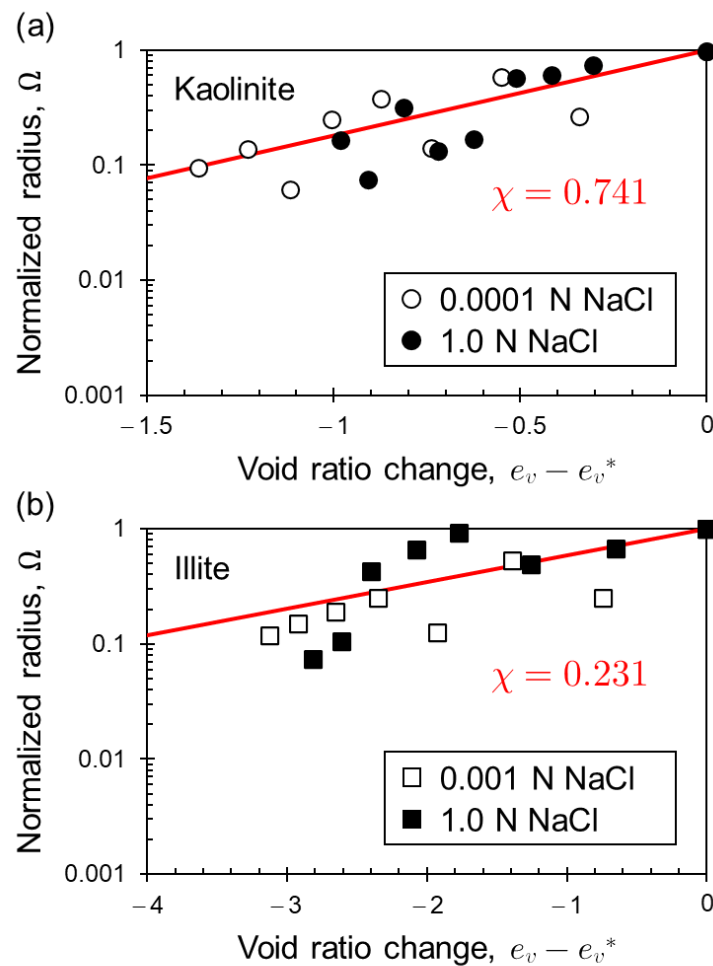$$\log_{10} \Omega = \log_{10}\left(\frac{a}{a^*}\right) = \chi(e_v - e_v{}^*) \tag{17}$$

where $e_v{}^*$ stands for a reference void ratio, $a^*$ for the corresponding capillary radius, and $\chi$ for a fitting parameter. Fitting curves and experimental data are shown in Figure 4. It is obvious that Equation (17) can capture the physical bases of the characteristic pore size change due to consolidation. The fitting parameter $\chi = 0.741$, $\chi = 0.231$, and $\chi = 0.0958$ for kaolinite, illite, and smectite minerals, respectively.



**Figure 3.** Comparisons of experimental and theoretical permeabilities of kaolinite (**a**), illite (**b**), and smectite (**c**) minerals when subjected to consolidation in an oedometer cell. The fitted capillary radius (i.e., the characteristic pore size) changes with the void ratio of kaolinite (**d**), illite (**e**), and smectite (**f**) minerals. The dimension N represents normality and, for the sodium chloride (NaCl) solution, 1.0 N stands for a mass concentration of 0.0585. The dimension mD represents millidarcy, and $1.0 \text{ mD} = 0.987 \times 10^{-15} \text{ m}^2$.

**Table 2.** Values of the Lin's Concordance Correlation Coefficient (LCCC).

| Experimental Conditions | LCCC | Figure | Reference |
|---|---|---|---|
| Kaolinite (0.0001 N NaCl)<br>Kaolinite (1.0 N NaCl) | 0.99982<br>0.99978 | Figure 3a | [45] |
| Illite (0.001 N NaCl)<br>Illite (1.0 N NaCl) | 0.99984<br>0.99997 | Figure 3b | |
| Smectite (0.001 N NaCl)<br>Smectite (0.1 N NaCl) | 0.99993<br>0.99999 | Figure 3c | |
| Bentonite A (D. I. Water)<br>Bentonite A (0.1 N NaCl)<br>Bentonite A (1.0 N NaCl) | 0.99982<br>0.99982<br>0.99980 | Figure 5a | [21] |
| Bentonite B (D. I. Water)<br>Bentonite B (0.1 N NaCl)<br>Bentonite B (1.0 N NaCl) | 0.99992<br>0.99980<br>0.99989 | Figure 5b | |
| Bentonite C (D. I. Water)<br>Bentonite C (0.1 N NaCl)<br>Bentonite C (1.0 N NaCl) | 0.99996<br>0.99962<br>0.99990 | Figure 5c | |
| Bentonite D (D. I. Water)<br>Bentonite D (0.1 N NaCl)<br>Bentonite D (1.0 N NaCl) | 0.99984<br>0.99974<br>0.99987 | Figure 5d | |



**Figure 4.** *Cont.*
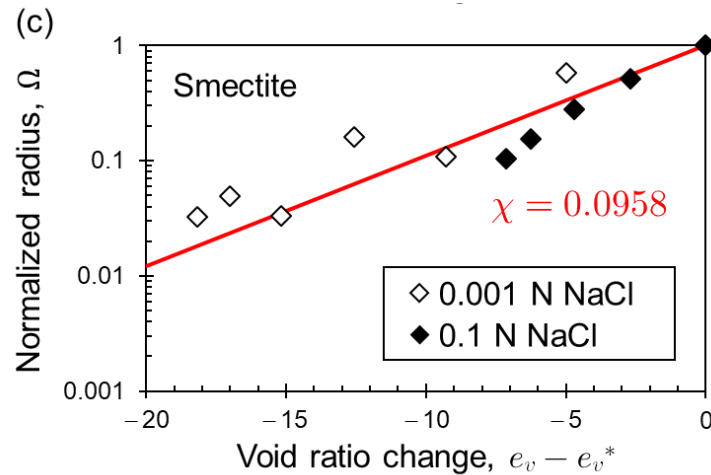
**Figure 4.** Normalized capillary radius $\Omega = \frac{a}{a^*}$ decreasing with decreasing void ratio change $e_v - e_v^*$ for kaolinite (**a**), illite (**b**), and smectite (**c**). The symbol $e_v^*$ stands for a reference void ratio, and $a^*$ represents the corresponding capillary radius. The red curve is drawn by Equation (17) with different values of the fitting parameter $\chi$.
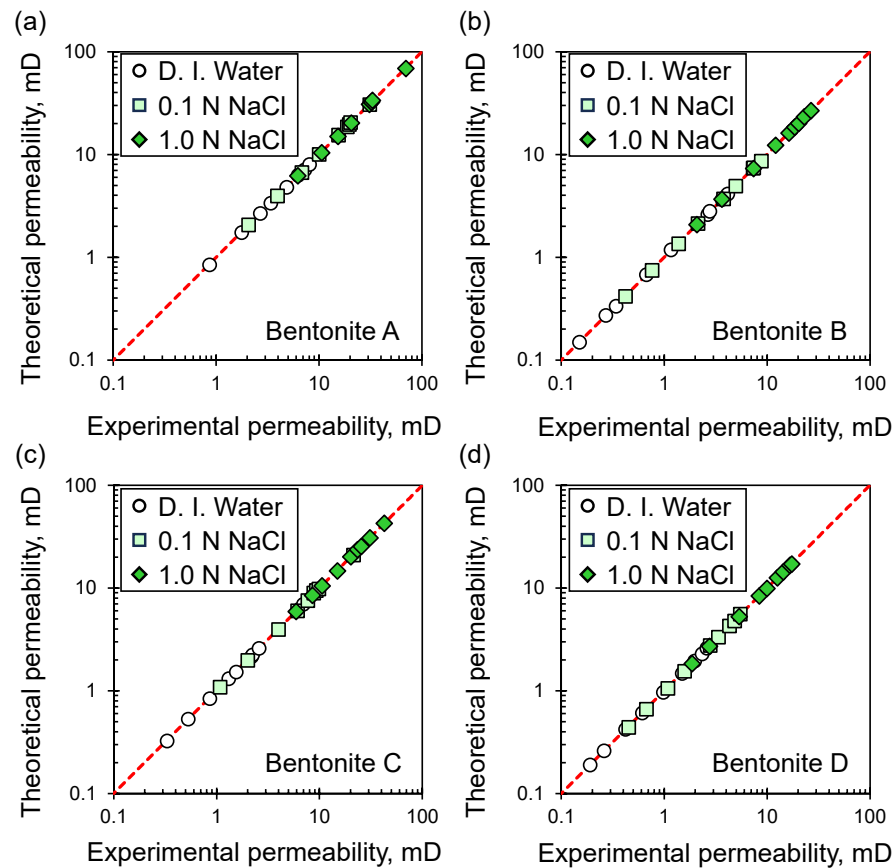


**Figure 5.** Comparisons of experimental and theoretical permeabilities of bentonites A (**a**), B (**b**), C (**c**), and D (**d**) when subjected to consolidation in an oedometer cell. The abbreviation "D. I. Water" in the legend denotes deionized water. The dimension N represents normality and, for the sodium chloride (NaCl) solution, 1.0 N stands for a mass concentration of 0.0585. The dimension mD represents millidarcy, and $1.0 \, \text{mD} = 0.987 \times 10^{-15} \, \text{m}^2$.

Mishra et al. [21] prepared samples of bentonite A, B, C, and D with the initial water content equal to their respective liquid limits and consolidated the samples in an oedometer cell with a diameter of 60 mm. The vertical loading increased from 4.9 kPa to 1.254 MPa

through seven steps with a unit incremental ratio, and the hydraulic conductivity of bentonites under different conditions of sodium chloride concentration is obtained according to the method used by Mesri and Olson [45]. The experimental results are used to further verify the model proposed in this study. All these bentonite samples are mixtures of basalt soil and bentonite with a mixing ratio of 100:20 by dry weight, and the liquid limit of all these samples ranges from 310.5% to 615.5%. The clay content of all these samples ranges from 61.4% to 82.8%, and the major mineral component of the clay is montmorillonite. Thus, the surface potential $\zeta$ of clay minerals is selected as $-19.3 \times 10^{-3}$ V [39] in this study.

Experimental and theoretical permeabilities are compared in Figure 5. It is obvious that the theoretical permeability is also very consistent with the experimental permeability for all these bentonites under different conditions of sodium chloride concentration, and all the LCCC values are larger than 0.999 (Table 2). The fitted capillary radius (i.e., the characteristic pore size) of all these bentonites is demonstrated in Figure 6. It is demonstrated that the fitted characteristic pore size mostly ranges from 0.1 μm to 1.6 μm for bentonite A (Figure 6a), from 0.03 μm to 0.84 μm for bentonite B (Figure 6b), from 0.04 μm to 1.05 μm for bentonite C (Figure 6c), and from 0.02 μm to 0.84 μm for bentonite D (Figure 6d). These values for the characteristic pore size are also quite comparable with the published data [48,49,68,69]. The fitted characteristic pore size also decreases with decreasing void ratio due to consolidation, and experimental data of the normalized capillary radius $\Omega$ together with fitting curves are shown in Figure 7. It is obvious that Equation (17) could also capture the physical bases of the characteristic pore size change due to consolidation. The fitting parameter $\chi = 1.123$, $\chi = 0.675$, $\chi = 0.811$, and $\chi = 0.438$ for bentonite A, B, C, and D, respectively.
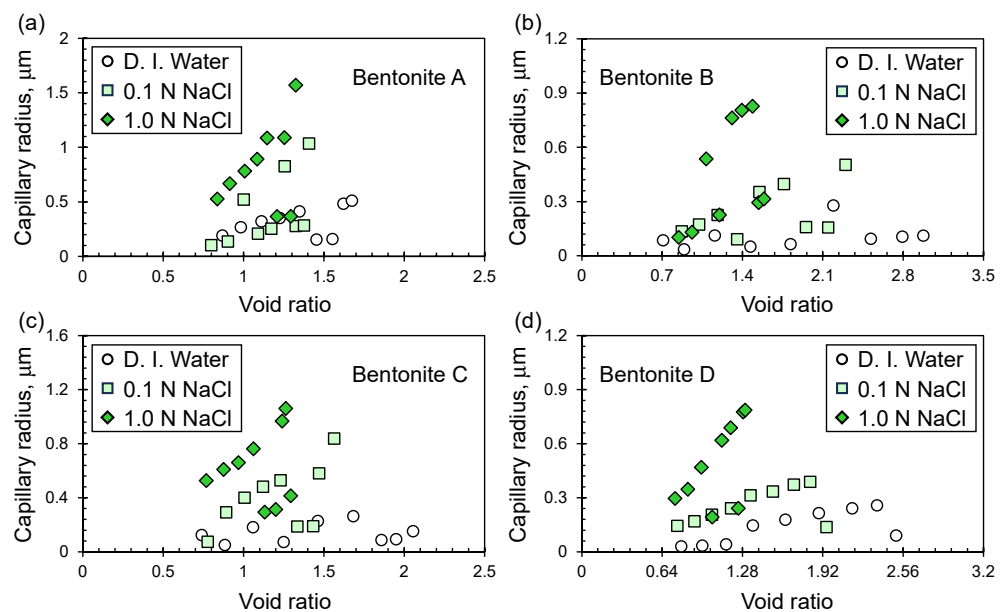


**Figure 6.** The fitted capillary radius (i.e., the characteristic pore size) changes with void ratio of bentonites A (**a**), B (**b**), C (**c**), and D (**d**). The abbreviation "D. I. Water" denotes deionized water. For the sodium chloride (NaCl) solution, the normality 1.0 N stands for a mass concentration of 0.0585.

In addition to the void ratio dependent data, Mishra et al. [21] provided the hydraulic conductivity of bentonites at a particular void ratio of 1.2 to show the dependence on the sodium chloride concentration. For each concentration, the fitted capillary radii corresponding to neighbor void ratios just lower and higher than 1.2 are used to calculate the hydraulic permeability of bentonites. The calculated results, together with corresponding experimental data, are shown in Figures 8 and 9. It is demonstrated that the experimental data of all these bentonites mostly occur between the theoretical results, which are acquired by using the lower and higher neighbor void ratios. This further demonstrates the capabil-

ity of the proposed model to predict the void ratio dependent hydraulic permeability of clayey sediments considering the impact of pore fluid chemistry.
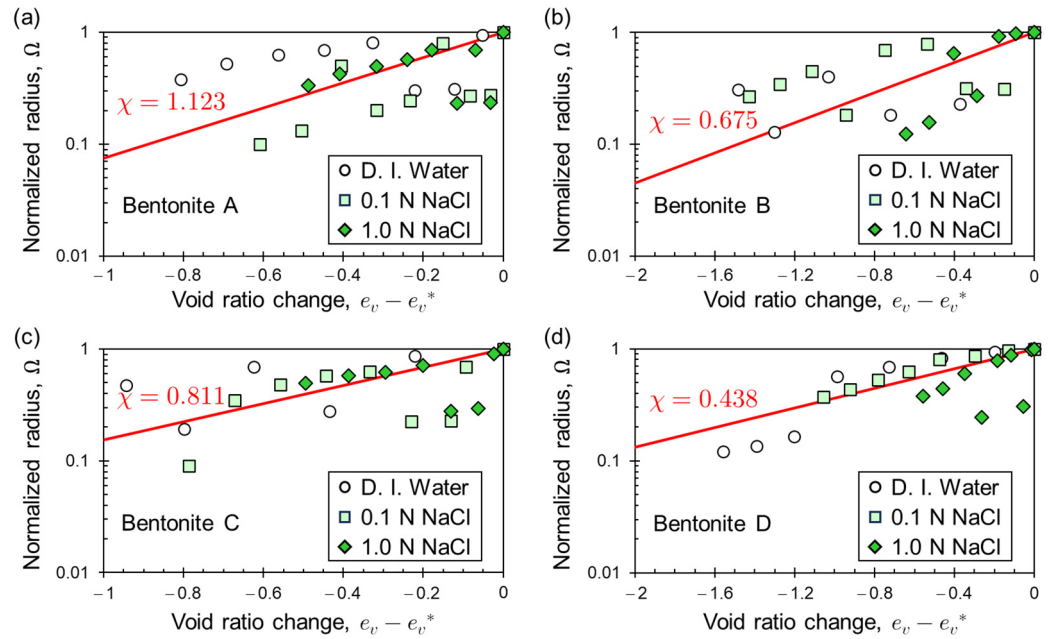


**Figure 7.** Normalized capillary radius $\Omega = \frac{a}{a^*}$ decreasing with decreasing void ratio change $e_v - e_v^*$ for bentonites A (**a**), B (**b**), C (**c**), and D (**d**). The symbol $e_v^*$ stands for a reference void ratio, and $a^*$ represents the corresponding capillary radius. The red curve is drawn by Equation (17) with different $\chi$ values.
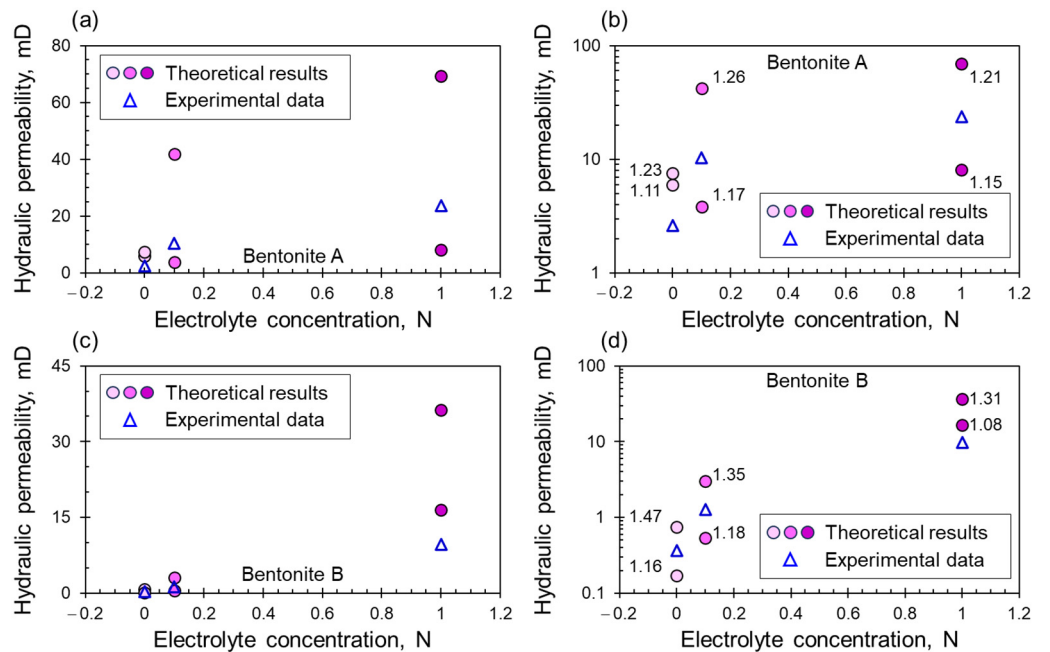


**Figure 8.** The electrolyte concentration-dependent hydraulic permeability of bentonites A (**a**,**b**) and B (**c**,**d**). The experimental data are obtained at a particular void ratio of 1.2, and the theoretical results are acquired by substituting lower and higher neighbor void ratios into the model. The lower and higher void ratios neighboring the void ratio of 1.2 are denoted as black decimals in the semilogarithmic coordinate system (**b**,**d**).
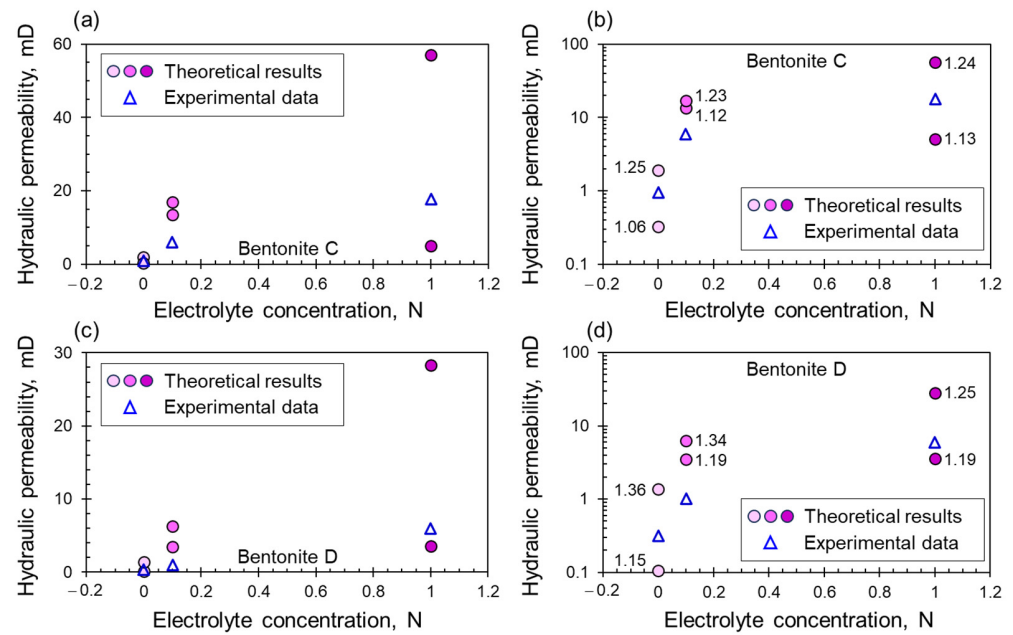
**Figure 9.** The electrolyte concentration dependent hydraulic permeability of bentonites C (**a**,**b**) and D (**c**,**d**). The experimental data are obtained at a particular void ratio of 1.2, and the theoretical results are acquired by substituting lower and higher neighbor void ratios into the model. The lower and higher void ratios neighboring the void ratio of 1.2 are denoted as black decimals in the semilogarithmic coordinate system (**b**,**d**).

## 4. Sensitivity Analysis

### 4.1. Effects of the Characteristic Pore Size

A dimensionless hydraulic permeability $\Pi = \frac{K}{\widetilde{K}}$ is defined to characterize the electrokinetic phenomena effect, and the symbol $\widetilde{K}$ represents the hydraulic permeability of clayey sediments when the electrokinetic phenomena are not considered. It is easy to deduce a brief formulation $\Pi = \Gamma^{-1}$. The normalized viscosity $\Gamma$ and the dimensionless hydraulic permeability $\Pi$, changing with the electrolyte concentration $n_0$ under different conditions of the capillary radius, are shown in Figure 10. It is demonstrated that the normalized viscosity $\Gamma$ and the dimensionless hydraulic permeability $\Pi$ are independent of the electrolyte concentration $n_0$ when the capillary radius $a$ (i.e., the characteristic pore size) is large (i.e., $a = 1.0 \, \mu$m) or small (i.e., $a = 0.0001 \, \mu$m). For the medium sized capillary radii, the normalized viscosity $\Gamma$ and the dimensionless hydraulic permeability $\Pi$ are dependent on the electrolyte concentration $n_0$. More specifically, the normalized viscosity $\Gamma$ decreases while the dimensionless hydraulic permeability $\Pi$ increases with increasing electrolyte concentration for $a = 0.1 \, \mu$m. For $a = 0.01 \, \mu$m, the normalized viscosity $\Gamma$ firstly increases and then decreases with increasing electrolyte concentration, but the dimensionless hydraulic permeability $\Pi$ changes inversely. With the capillary radius further decreasing to $a = 0.001 \, \mu$m, the normalized viscosity $\Gamma$ increases, while the dimensionless hydraulic permeability $\Pi$ decreases with increasing electrolyte concentration.

The dimensionless capillary radius $\kappa a$ and the hydraulic permeability $K$, changing with the electrolyte concentration $n_0$, are shown in Figure 11. It is demonstrated that the dimensionless capillary radius $\kappa a$ is far from the unit line for $a = 1.0 \, \mu$m and $a = 0.0001 \, \mu$m. For the medium sized capillary radii, the dimensionless capillary radius $\kappa a$ approaches the unit line to some extent, or even crosses the unit line ($a = 0.01 \, \mu$m). This indicates that effects of the electrokinetic phenomena are significant when the dimensionless capillary radius $\kappa a$ is close to the unit, and the effects should be considered. The capillary radius $a$ largely controls the hydraulic permeability of clayey sediments. When the capillary radius is unchanged, the hydraulic permeability changes along with the electrolyte concentration

are small. It could be inferred that the characteristic pore size is not only a major factor denoting effects of the electrokinetic phenomena but also directly controls the hydraulic permeability of clayey sediments.
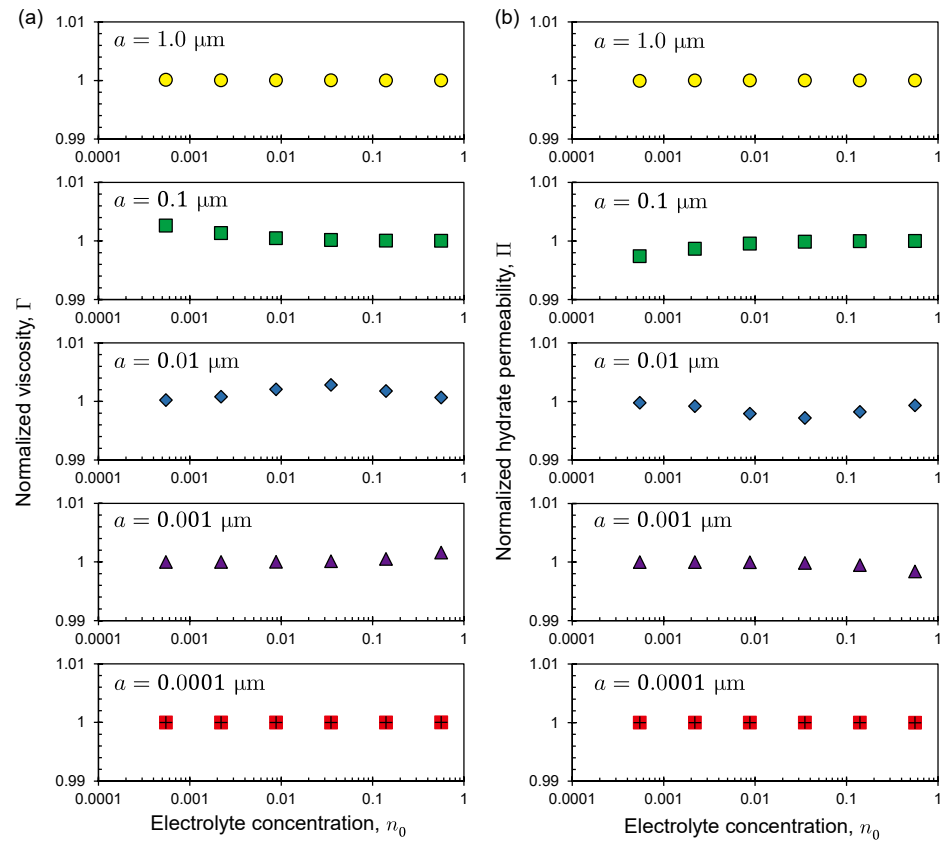


**Figure 10.** The normalized viscosity $\Gamma$ (**a**) and the normalized hydraulic permeability $\Pi$ (**b**) changes with the electrolyte concentration $n_0$ under different conditions of the capillary radius $a$.
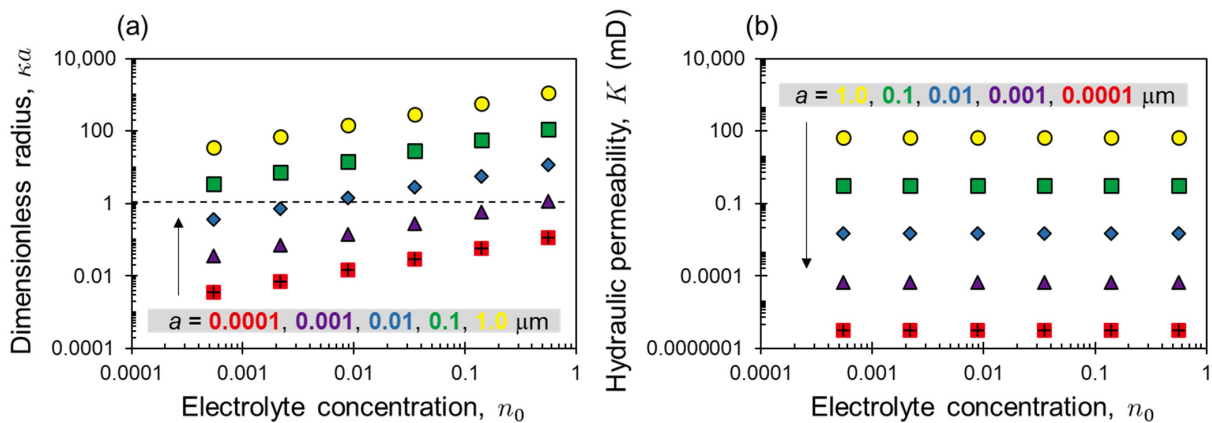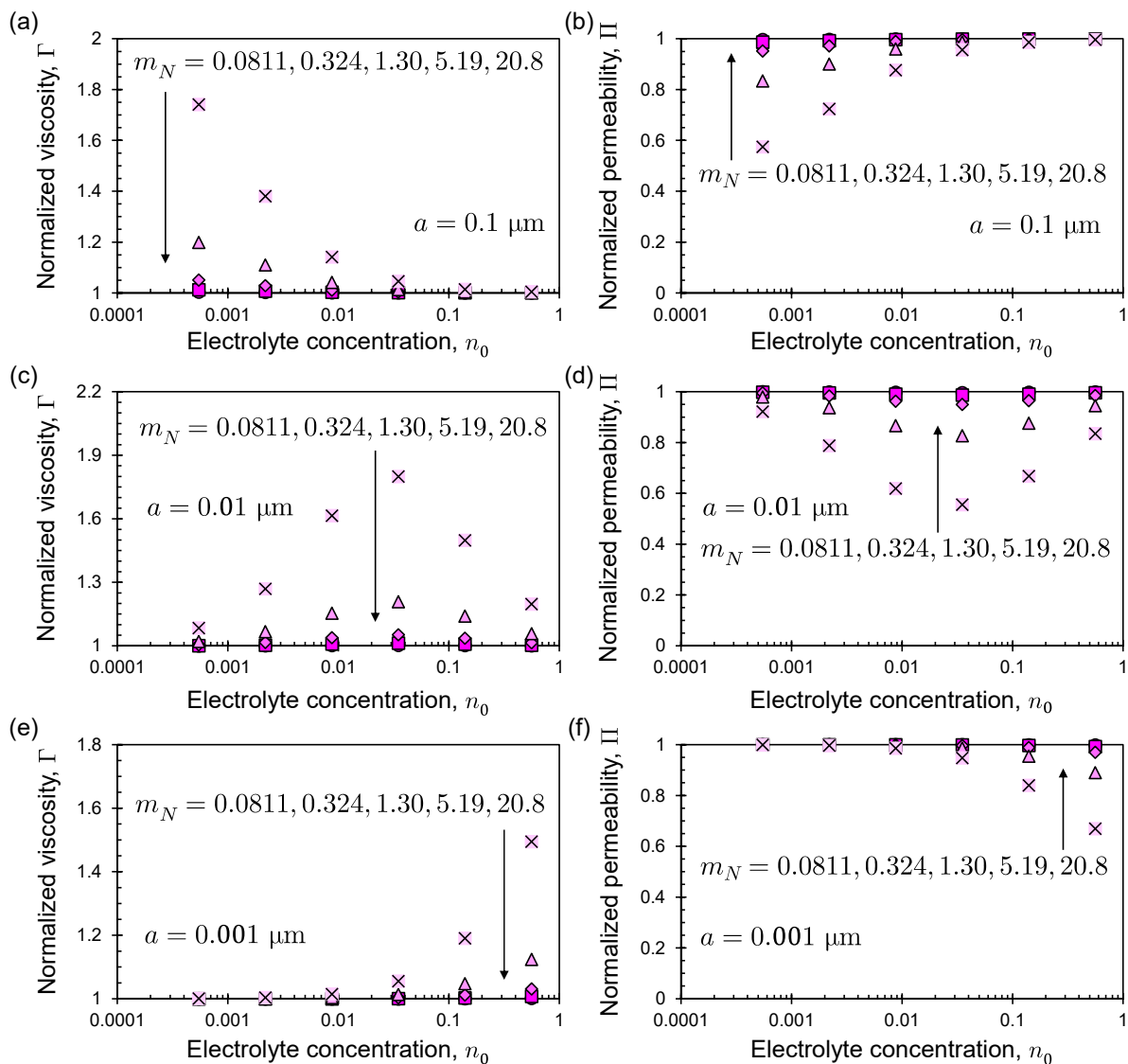


**Figure 11.** The dimensionless capillary radius $\kappa a$ (**a**) and the hydraulic permeability $K$ (**b**) changes with the electrolyte concentration $n_0$ under different conditions of the capillary radius $a$.
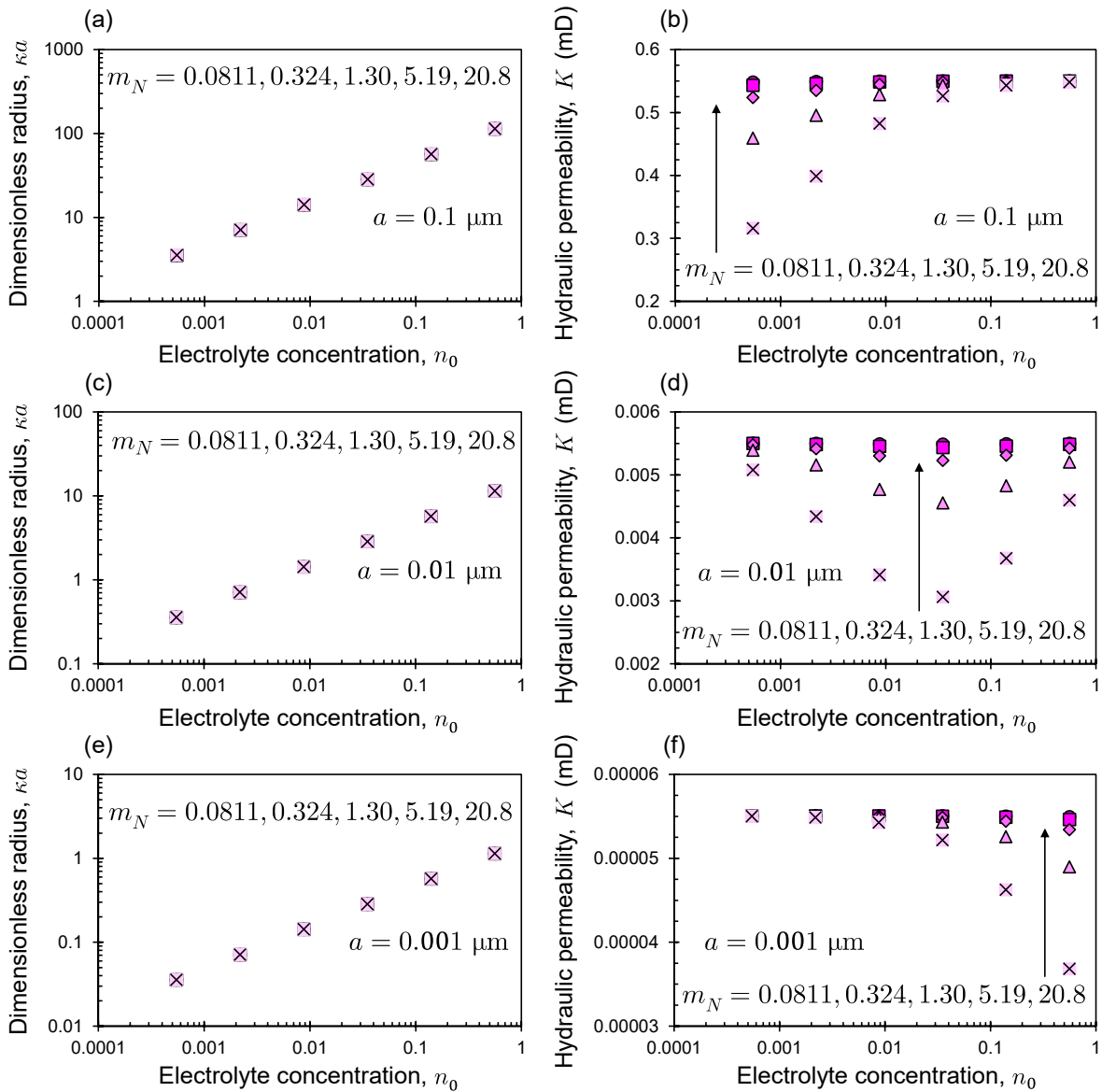
### 4.2. Effects of Ion Mobility

The normalized viscosity $\Gamma$ and the dimensionless hydraulic permeability $\Pi$, changing with the electrolyte concentration $n_0$ under different conditions of ion mobility, are shown in Figure 12. It is demonstrated that the normalized viscosity $\Gamma$ decreases (Figure 12a), while the dimensionless hydraulic permeability $\Pi$ increases (Figure 12b) with increasing electrolyte concentration for $a = 0.1$ μm. For $a = 0.01$ μm, the normalized viscosity $\Gamma$ firstly increases and then

decreases (Figure 12c) with increasing electrolyte concentration, but the dimensionless hydraulic permeability $\Pi$ firstly decreases and then increases (Figure 12d) with increasing electrolyte concentration. The normalized viscosity $\Gamma$ increases (Figure 12e), while the dimensionless hydraulic permeability $\Pi$ decreases (Figure 12f) with increasing electrolyte concentration for $a = 0.001$ μm. These responses to the electrolyte concentration change become much stronger when a smaller ion mobility is applied. The dimensionless capillary radius $\kappa a$ and the hydraulic permeability $K$, changing with the electrolyte concentration $n_0$, are shown in Figure 13. It is obvious that the dimensionless capillary radius $\kappa a$ increases with increasing electrolyte concentration, and the change process is independent of the ion mobility (Figure 13a,c,e). The hydraulic permeability $K$ decreases (Figure 13b) with increasing electrolyte concentration for $a = 0.1$ μm. The hydraulic permeability $K$ firstly decreases and then increases (Figure 13d) with increasing electrolyte concentration for $a = 0.01$ μm. The hydraulic permeability $K$ decreases (Figure 13f) with increasing electrolyte concentration for $a = 0.001$ μm. In addition, the maximal change in hydraulic permeability decreases with increasing ion mobility.



**Figure 12.** The normalized viscosity $\Gamma$ (**a**,**c**,**e**) and the normalized hydraulic permeability $\Pi$ (**b**,**d**,**f**) change with the electrolyte concentration $n_0$ under different conditions of dimensionless ion mobility $m_N = \frac{m}{m^*}$, where $m^* = 1.0 \times 10^{-8}$ m$^2$s$^{-1}$V$^{-1}$. The capillary radius $a = 0.1$ μm (**a**,**b**), $a = 0.01$ μm (**c**,**d**), and $a = 0.001$ μm (**e**,**f**).

**Figure 13.** The dimensionless capillary radius $\kappa a$ (**a**,**c**,**e**) and the hydraulic permeability $K$ (**b**,**d**,**f**) change with the electrolyte concentration $n_0$ under different conditions of the dimensionless ion mobility $m_N = \frac{m}{m^*}$, where $m^* = 1.0 \times 10^{-8}$ m$^2$s$^{-1}$V$^{-1}$. The capillary radius $a = 0.1$ μm (**a**,**b**), $a = 0.01$ μm (**c**,**d**), and $a = 0.001$ μm (**e**,**f**).

### 4.3. Effects of the Surface Dielectric Potential

The normalized viscosity $\Gamma$, the dimensionless hydraulic permeability $\Pi$, the dimensionless capillary radius $\kappa a$, and the hydraulic permeability $K$, changing with the electrolyte concentration $n_0$ under different conditions of the surface dielectric potential $\zeta$, are shown in Figure 14. It is demonstrated that the normalized viscosity $\Gamma$ firstly increases and then decreases (Figure 14a), the dimensionless hydraulic permeability $\Pi$ firstly decreases and then increases (Figure 14b), the dimensionless capillary radius $\kappa a$ increases (Figure 14c), and the hydraulic permeability $K$ firstly decreases and then increases (Figure 14d) with increasing electrolyte concentration. The maximal change in the normalized viscosity $\Gamma$, dimensionless hydraulic permeability $\Pi$, and the hydraulic permeability $K$ decreases with increasing surface dielectric potential $\zeta$. In addition, dependence of the dimensionless capillary radius on the electrolyte concentration is unchanged when different values are assigned to the surface dielectric potential.
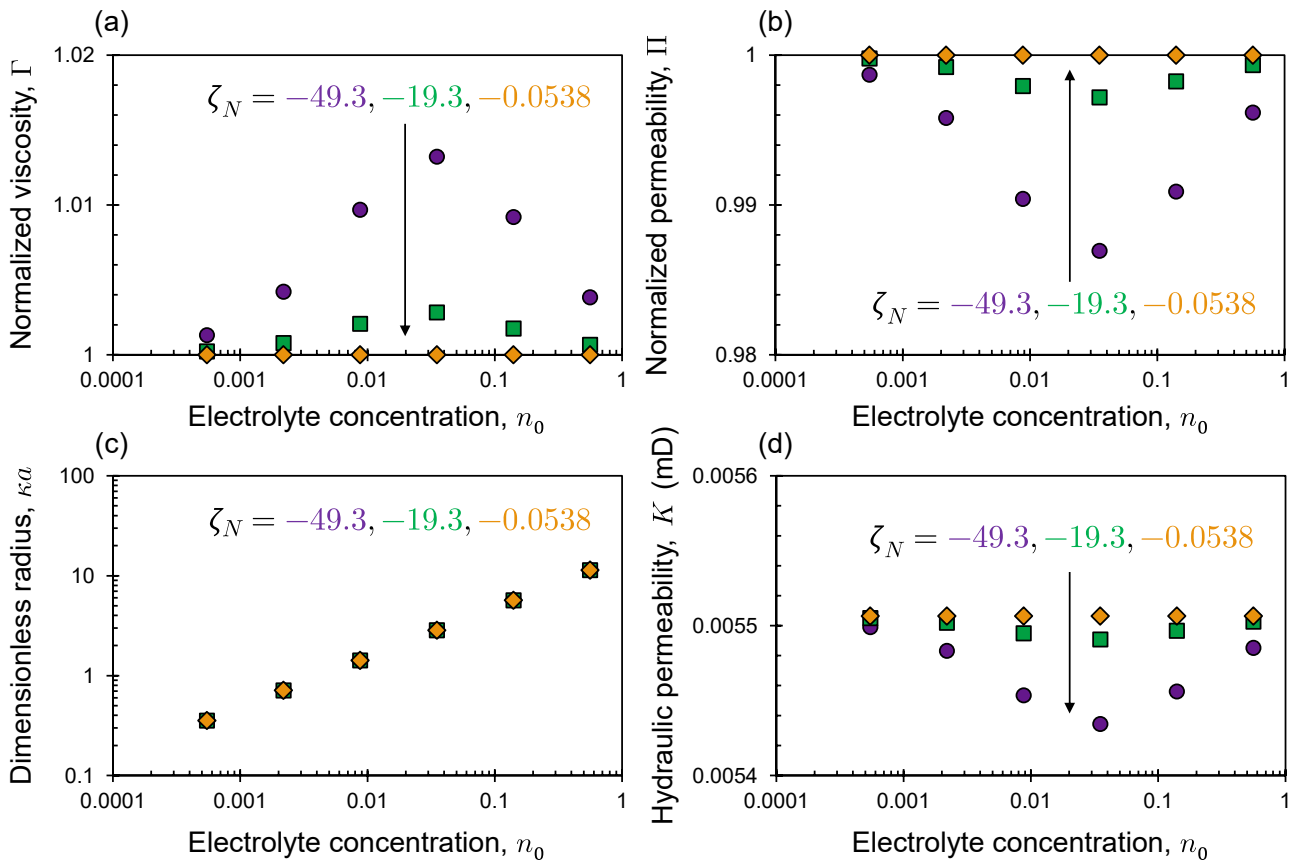
**Figure 14.** The normalized viscosity $\Gamma$ (**a**), the normalized hydraulic permeability $\Pi$ (**b**), the dimensionless capillary radius $\kappa a$ (**c**), and the hydraulic permeability $K$ (**d**), changing with the electrolyte concentration $n_0$ under different conditions of the dimensionless surface dielectric potential $\zeta_N = \frac{\zeta}{\zeta^*}$, where $\zeta^* = 1.0 \times 10^{-3}$ V. The capillary radius $a = 0.01$ μm.

## 5. Discussion

Depressurization is currently a preferred method to recover natural gas from hydrate deposits in the ocean, and marine sediments surrounding the wellbore experience pore fluid chemistry changes (e.g., desalination) and increased effective stress, which causes further consolidation. During the consolidation, the characteristic pore size of marine sediments generally decreases. Results of the sensitivity analyses have shown that the decreased characteristic pore size and the decreased pore fluid salinity could jointly affect the hydraulic permeability of clayey sediments, and the coupling effects of pore fluid desalination and increased effective stress during gas hydrate production by depressurization are discussed in this section.
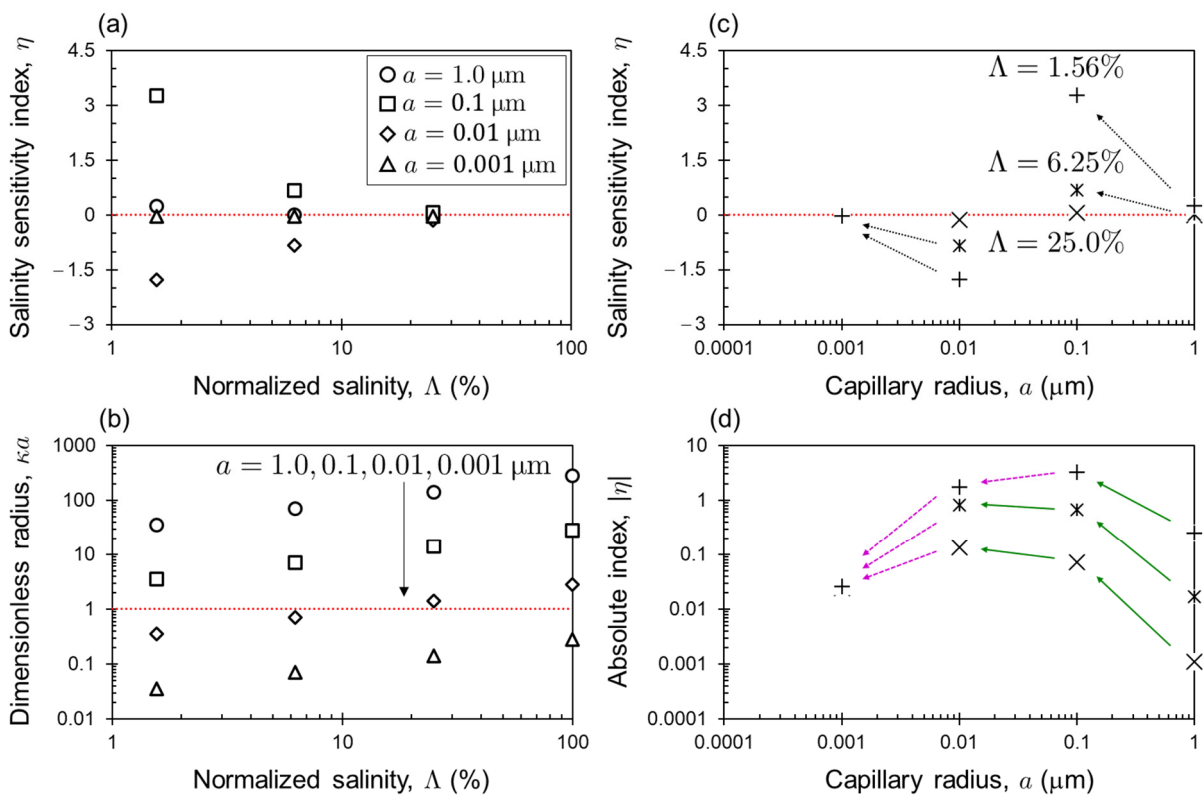
Dependence of the hydraulic permeability $K$ on pore fluid salinity $c_0$ is characterized by defining a salinity sensitivity index $\eta$ as

$$\eta = \frac{1}{K}\frac{\partial K}{\partial c_0} \tag{18}$$

If values of the salinity sensitivity index are negative, it is indicated that the hydraulic permeability increases when the pore fluid salinity decreases (i.e., negatively correlated). Positive values of the salinity sensitivity index mean that the hydraulic permeability is positively correlated to the pore fluid salinity. Whether the values are negative or positive, the larger the absolute value of the salinity sensitivity index, the higher the level of the salinity sensitivity of the hydraulic permeability.

The salinity sensitivity index $\eta$, changing with the normalized pore fluid salinity $\Lambda$ under different conditions of the capillary radius $a$, is demonstrated in Figure 15a. The

normalized pore fluid salinity $\Lambda$ is defined as the ratio of the pore fluid salinity after desalination over the original pore fluid salinity (i.e., the seawater salinity), and $\Lambda = 100\%$ indicates that the seawater has not been desalinized. It is demonstrated that the salinity sensitivity index $\eta$ barely changes with the normalized salinity $\Lambda$ for $a = 0.001$ μm. When the capillary radius increases to $a = 0.01$ μm, the salinity sensitivity index $\eta$ decreases with decreasing normalized salinity $\Lambda$ (i.e., increasing desalination degree). The salinity sensitivity index $\eta$ obviously increases with decreasing normalized salinity $\Lambda$ for $a = 0.1$ μm. When the capillary radius further increases to $a = 1.0$ μm, the salinity sensitivity index $\eta$ slightly increases with decreasing normalized salinity desalination degree $\Lambda$. These responses could be explained by the dimensionless capillary radius change (Figure 15b). It is demonstrated that the dimensionless capillary radius for $a = 1.0$ μm is much larger than the unit, and the dimensionless capillary radius for $a = 0.001$ μm is much smaller than the unit. For medium-sized capillary radii (i.e., $a = 0.1$ μm and $a = 0.01$ μm), the dimensionless capillary radius is much closer to the unit. The salinity sensitivity index $\eta$ and its absolute value $|\eta|$, changing with the capillary radius $a$, are shown in Figure 15c,d, respectively. It is demonstrated that the salinity sensitivity index $\eta$ increases when the capillary radius decreases from $a = 1.0$ μm to $a = 0.1$ μm and from $a = 0.01$ μm to $a = 0.001$ μm. However, when the capillary radius decreases from $a = 0.1$ μm to $a = 0.01$ μm, the salinity sensitivity index $\eta$ decreases. In addition, the absolute salinity sensitivity index $|\eta|$ increases when the capillary radius decreases from $a = 1.0$ μm to $a = 0.1$ μm and decreases when the capillary radius decreases from $a = 0.01$ μm to $a = 0.001$ μm. This indicates that the salinity sensitivity of the hydraulic permeability is characteristic pore size dependent, and whether the salinity sensitivity becomes stronger or weaker highly depends on the original characteristic pore size of clayey sediments when subjected to consolidation.



**Figure 15.** The salinity sensitivity index $\eta$ of the hydraulic permeability (**a**) and the dimensionless capillary radius $\kappa a$ (**b**) change with the normalized pore fluid salinity $\Lambda$ under different conditions of the capillary radius $a$. The salinity sensitivity index $\eta$ (**c**) and its absolute value $|\eta|$ (**d**) change with the capillary radius $a$.

## 6. Conclusions

This study derives and verifies a theoretical model for the hydraulic permeability of clayey sediments, and the verified model is used as a base for sensitivity analyses to deepen the understanding of how hydraulic permeability depends on the pore fluid salinity. Results are further extended to discuss responses of the hydraulic permeability to combined changes in the effective stress and pore fluid salinity during gas hydrate production. The main conclusions are drawn as follows:

The hydraulic permeability of clayey sediments saturated with a saline solution is reduced, due to the development of an electric double layer near the surface of clay minerals, and the permeability reduction is significant only when the electric double layer thickness is comparable to the characteristic pore size. In addition, a smaller ion mobility of the saline solution and a lower surface dielectric potential of the clay minerals both lead to a bigger reduction in hydraulic permeability.

During hydrate production by depressurization in the ocean, sensitivity of the hydraulic permeability to the decreasing salinity of seawater within marine sediments is dependent on the desalination degree and the reduction history of pore sizes. When subjected to a desalination of seawater within marine sediments, with decreasing void ratio due to consolidation, the salinity sensitivity becomes stronger if the original characteristic pore size is relatively large (e.g., several microns) but becomes weaker if relatively small (e.g., several nanometers).

Although the pore size distribution and the fabric of clay particles are excluded, the theoretical model could certainly calculate the macroscopic hydraulic permeability of clayey sediments from the microscopic thickness of an electric double layer near the surface of clay minerals. Impacts of the pore fluid chemistry are properly considered, and the theoretical model has significant potential in gas hydrate production and seawater intrusion prevention.

## References

1. Kumari, N.; Mohan, C. Basics of Clay Minerals and Their Characteristic Properties. In *Clay and Clay Minerals*; IntechOpen: London, UK, 2021; ISBN 978-1-83969-564-3.
2. Ghosh, B.; Chakraborty, D. An Overview of the Clay Minerals: Composition, Classification, Internal Structure and Properties. In *Clay Minerals: Their Antimicrobial and Antitoxic Applications*; Ghosh, B., Chakraborty, D., Eds.; Springer International Publishing: Cham, Switzerland, 2023; pp. 1–24. ISBN 978-3-031-22327-3.
3. Iranfar, S.; Karbala, M.M.; Shakiba, M.; Shahsavari, M.H. Effects of Type and Distribution of Clay Minerals on the Physico-Chemical and Geomechanical Properties of Engineered Porous Rocks. *Sci. Rep.* **2023**, *13*, 5837. [CrossRef] [PubMed]
4. Brown, G. Structure, Crystal Chemistry, and Origin of the Phyllosilicate Minerals Common in Soil Clays. In *Soil Colloids and Their Associations in Aggregates*; De Boodt, M.F., Hayes, M.H.B., Herbillon, A., De Strooper, E.B.A., Tuck, J.J., Eds.; Springer US: Boston, MA, USA, 1990; pp. 7–38. ISBN 978-1-4899-2611-1.

5. Fagel, N. Chapter Four Clay Minerals, Deep Circulation and Climate. In *Developments in Marine Geology*; Hillaire–Marcel, C., De Vernal, A., Eds.; Proxies in Late Cenozoic Paleoceanography; Elsevier: Amsterdam, The Netherlands, 2007; Volume 1, pp. 139–184.

6. Thiry, M. Palaeoclimatic Interpretation of Clay Minerals in Marine Deposits: An Outlook from the Continental Origin. *Earth-Sci. Rev.* **2000**, *49*, 201–221. [CrossRef]

7. Jang, J.; Cao, S.C.; Stern, L.A.; Jung, J.; Waite, W.F. Impact of Pore-Fluid Chemistry on Fine-Grained Sediment Fabric and Compressibility. *J. Geophys. Res. Solid. Earth* **2018**, *123*, 5495–5514. [CrossRef]

8. Li, Y.; Liu, L.; Jin, Y.; Wu, N. Characterization and Development of Marine Natural Gas Hydrate Reservoirs in Marine Clayey-Silt Reservoirs: A Review and Discussion. *Adv. Geo-Energy Res.* **2021**, *5*, 75–86. [CrossRef]

9. Boswell, R. Is Gas Hydrate Energy Within Reach? *Science* **2009**, *325*, 957–958. [CrossRef]

10. Sloan, E.D. Fundamental Principles and Applications of Natural Gas Hydrates. *Nature* **2003**, *426*, 353–363. [CrossRef]

11. Cunillera-Montcusí, D.; Beklioğlu, M.; Cañedo-Argüelles, M.; Jeppesen, E.; Ptacnik, R.; Amorim, C.A.; Arnott, S.E.; Berger, S.A.; Brucet, S.; Dugan, H.A.; et al. Freshwater Salinisation: A Research Agenda for a Saltier World. *Trends Ecol. Evol.* **2022**, *37*, 440–453. [CrossRef]

12. Post, V.E.A.; Groen, J.; Kooi, H.; Person, M.; Ge, S.; Edmunds, W.M. Offshore Fresh Groundwater Reserves as a Global Phenomenon. *Nature* **2013**, *504*, 71–78. [CrossRef]

13. Fang, Y.; Zheng, T.; Wang, H.; Zheng, X.; Walther, M. Influence of Dynamically Stable-Unstable Flow on Seawater Intrusion and Submarine Groundwater Discharge Over Tidal and Seasonal Cycles. *J. Geophys. Res. Ocean* **2022**, *127*, e2021JC018209. [CrossRef]

14. Werner, A.D.; Bakker, M.; Post, V.E.A.; Vandenbohede, A.; Lu, C.; Ataie-Ashtiani, B.; Simmons, C.T.; Barry, D.A. Seawater Intrusion Processes, Investigation and Management: Recent Advances and Future Challenges. *Adv. Water Resour.* **2013**, *51*, 3–26. [CrossRef]

15. Deng, Y.; Zhang, T.; Cui, Y.; Chen, Y.; Deng, T.; Zhou, X. Pore Water Salinity Effect on the Intrinsic Compression Behaviour of Artificial Soft Soils. *Appl. Clay Sci.* **2018**, *166*, 299–306. [CrossRef]

16. Musso, G.; Scelsi, G.; Della Vecchia, G. Chemo-Mechanical Behaviour of Non-Expansive Clays Accounting for Salinity Effects. *Géotechnique* **2024**, *74*, 632–646. [CrossRef]

17. Song, M.-M.; Zeng, L.-L.; Hong, Z.-S. Pore Fluid Salinity Effects on Physicochemical-Compressive Behaviour of Reconstituted Marine Clays. *Appl. Clay Sci.* **2017**, *146*, 270–277. [CrossRef]

18. Tang, S.; She, D.; Wang, H. Effect of Salinity on Soil Structure and Soil Hydraulic Characteristics. *Can. J. Soil. Sci.* **2021**, *101*, 62–73. [CrossRef]

19. Cai, W.; Bordoloi, S.; Zhu, C.; Gupt, C.B. Influence of Plasticity and Porewater Salinity on Shrinkage and Water Retention Characteristics of Biochar-Engineered Clays. *Soil Sci. Soc. Am. J.* **2023**, *87*, 1285–1303. [CrossRef]

20. Bayesteh, H.; Hezareh, H. Behavior of Cement-Stabilized Marine Clay and Pure Clay Minerals Exposed to High Salinity Grout. *Constr. Build. Mater.* **2023**, *383*, 131334. [CrossRef]

21. Mishra, A.K.; Ohtsubo, M.; Li, L.Y.; Higashi, T.; Park, J. Effect of Salt of Various Concentrations on Liquid Limit, and Hydraulic Conductivity of Different Soil-Bentonite Mixtures. *Environ. Geol.* **2009**, *57*, 1145–1153. [CrossRef]

22. Quirk, J.P.; Schofield, R.K. The Effect of Electrolyte Concentration on Soil Permeability. *J. Soil. Sci.* **1955**, *6*, 163–178. [CrossRef]

23. Jo, H.Y.; Benson, C.H.; Edil, T.B. Hydraulic Conductivity and Cation Exchange in Non-Prehydrated and Prehydrated Bentonite Permeated with Weak Inorganic Salt Solutions. *Clays Clay Miner.* **2004**, *52*, 661–679. [CrossRef]

24. Yilmaz, G.; Yetimoglu, T.; Arasan, S. Hydraulic Conductivity of Compacted Clay Liners Permeated with Inorganic Salt Solutions. *Waste Manag. Res.* **2008**, *26*, 464–473. [CrossRef]

25. Wan, Y.; Yuan, Y.; Zhou, C.; Liu, L. Multiphysics Coupling in Exploitation and Utilization of Geo-Energy: State-of-the-Art and Future Perspectives. *Adv. Geo-Energy Res.* **2023**, *10*, 7–13. [CrossRef]

26. Liu, L.; Lu, X.; Zhang, X. A Theoretical Model for Predicting the Spatial Distribution of Gas Hydrate Dissociation under the Combination of Depressurization and Heating without the Discontinuous Interface Assumption. *J. Pet. Sci. Eng.* **2015**, *133*, 589–601. [CrossRef]

27. Zhang, H.; Bian, H.; Qi, S.; Wang, J. A Comprehensive Analysis of Formation Conditions, Intrinsic Properties, and Mechanical Responses of Gas Hydrate-Bearing Sediments. *Rock Mech. Bull.* **2024**, *3*, 100114. [CrossRef]

28. Strack, O.D.L.; Stoeckl, L.; Damm, K.; Houben, G.; Ausk, B.K.; de Lange, W.J. Reduction of Saltwater Intrusion by Modifying Hydraulic Conductivity. *Water Resour. Res.* **2016**, *52*, 6978–6988. [CrossRef]

29. Kerrou, J.; Renard, P. A Numerical Analysis of Dimensionality and Heterogeneity Effects on Advective Dispersive Seawater Intrusion Processes. *Hydrogeol. J.* **2010**, *18*, 55–72. [CrossRef]

30. Lu, C.; Chen, Y.; Zhang, C.; Luo, J. Steady-State Freshwater–Seawater Mixing Zone in Stratified Coastal Aquifers. *J. Hydrol.* **2013**, *505*, 24–34. [CrossRef]

31. Liu, L.; Dai, S.; Ning, F.; Cai, J.; Liu, C.; Wu, N. Fractal Characteristics of Unsaturated Sands—Implications to Relative Permeability in Hydrate-Bearing Sediments. *J. Nat. Gas. Sci. Eng.* **2019**, *66*, 11–17. [CrossRef]

32. Golparvar, A.; Zhou, Y.; Wu, K.; Ma, J.; Yu, Z. A Comprehensive Review of Pore Scale Modeling Methodologies for Multiphase Flow in Porous Media. *Adv. Geo-Energy Res.* **2018**, *2*, 418–440. [CrossRef]

33. Pisano, A. From Tubes and Catheters to the Basis of Hemodynamics: The Hagen–Poiseuille Equation. In *Physics for Anesthesiologists: From Daily Life to the Operating Room*; Pisano, A., Ed.; Springer International Publishing: Cham, Switzerland, 2017; pp. 55–61. ISBN 978-3-319-57330-4.

34. Darcy, H. *The Public Fountains of the City of Dijon (Translated by Patricia Bobeck)*; Kendall Hunt Publishing Co.: Dubuque, IA, USA, 2004; ISBN 978-0-7575-0540-9.
35. Brown, G.O. Henry Darcy and the Making of a Law. *Water Resour. Res.* **2002**, *38*, 11-1–11-12. [CrossRef]
36. Kozeny, J. Uber Kapillare Leitung Des Wassers Im Boden. *Sitzungsberichte Der Akad. Der Wiss. Math.-Naturwissenschaftliche Kl.* **1927**, *136*, 271–306.
37. Carman, P.C. Fluid Flow through Granular Beds. *Trans. Inst. Chem. Eng.* **1937**, *15*, 150–167. [CrossRef]
38. Chapuis, R.P. Predicting the Saturated Hydraulic Conductivity of Soils: A Review. *Bull. Eng. Geol. Environ.* **2012**, *71*, 401–434. [CrossRef]
39. Qin, Z.; Nie, X.; Yu, W.; Yang, S.; Zhou, Z.; Yang, S.; Wan, Q. Probing the Surface Electrical Properties of Clay Minerals with Electrostatic Force Microscopy and Kelvin Probe Force Microscopy. *Mater. Res. Express* **2024**, *11*, 025501. [CrossRef]
40. Carcione, J.M.; Gei, D.; Yu, T.; Ba, J. Effect of Clay and Mineralogy on Permeability. *Pure Appl. Geophys.* **2019**, *176*, 2581–2594. [CrossRef]
41. Akin, I.D.; Likos, W.J. Single-Point and Multi-Point Water-Sorption Methods for Specific Surface Areas of Clay. *Geotech. Test. J.* **2016**, *39*, 291–300. [CrossRef]
42. Maček, M.; Mauko, A.; Mladenovič, A.; Majes, B.; Petkovšek, A. A Comparison of Methods Used to Characterize the Soil Specific Surface Area of Clays. *Appl. Clay Sci.* **2013**, *83–84*, 144–152. [CrossRef]
43. Sharma, A.; Hazra, B.; Spagnoli, G.; Sekharan, S. Probabilistic Estimation of Specific Surface Area and Cation Exchange Capacity: A Global Multivariate Distribution. *Can. Geotech. J.* **2021**, *58*, 1077–1094. [CrossRef]
44. Taylor, D.W. Fundamentals of Soil Mechanics. *Soil Sci.* **1948**, *66*, 161. [CrossRef]
45. Mesri, G.; Olson, R.E. Mechanisms Controlling the Permeability of Clays. *Clays Clay Miner.* **1971**, *19*, 151–158. [CrossRef]
46. Nagaraj, T.S.; Pandian, N.S.; Narashimha Raju, P.S.R. Stress State-Permeability Relationships for Fine-Grained Soils. *Géotechnique* **1993**, *43*, 333–336. [CrossRef]
47. Dai, S.; Santamarina, J.C. *Hydrate-Bearing Clayey Sediments: Morphology, Physical Properties, Production and Engineering/Geological Implications*; Georgia Institute of Technology: Atlanta, GA, USA, 2017.
48. Diamond, S. Pore Size Distributions in Clays. *Clays Clay Miner.* **1970**, *18*, 7–23. [CrossRef]
49. Zhang, X.; Wang, G.; Liu, X.; Xu, Y.; Kong, L. Microstructural Analysis of Pore Characteristics of Natural Structured Clay. *Bull. Eng. Geol. Environ.* **2022**, *81*, 473. [CrossRef]
50. van der Heyden, F.H.J.; Bonthuis, D.J.; Stein, D.; Meyer, C.; Dekker, C. Power Generation by Pressure-Driven Transport of Ions in Nanofluidic Channels. *Nano Lett.* **2007**, *7*, 1022–1025. [CrossRef]
51. Wu, J. Understanding the Electric Double-Layer Structure, Capacitance, and Charging Dynamics. *Chem. Rev.* **2022**, *122*, 10821–10859. [CrossRef] [PubMed]
52. Olthuis, W.; Schippers, B.; Eijkel, J.; van den Berg, A. Energy from Streaming Current and Potential. *Sens. Actuators B Chem.* **2005**, *111–112*, 385–389. [CrossRef]
53. Yang, J.; Kwok, D.Y. Microfluid Flow in Circular Microchannel with Electrokinetic Effect and Navier's Slip Condition. *Langmuir* **2003**, *19*, 1047–1053. [CrossRef]
54. Levine, S.; Marriott, J.R.; Neale, G.; Epstein, N. Theory of Electrokinetic Flow in Fine Cylindrical Capillaries at High Zeta-Potentials. *J. Colloid Interface Sci.* **1975**, *52*, 136–149. [CrossRef]
55. Bhattacharyya, A.; Masliyah, J.H.; Yang, J. Oscillating Laminar Electrokinetic Flow in Infinitely Extended Circular Microchannels. *J. Colloid Interface Sci.* **2003**, *261*, 12–20. [CrossRef]
56. Cheng, H.; Wang, F.; Guan, X.; Yang, G.; Yuan, Y.; Feng, G. A Mathematical Model for Pre-Darcy Flow in Low Permeability Porous Media with Stress Sensitivity and the Boundary-Layer Effect. *Eng. Geol.* **2023**, *324*, 107257. [CrossRef]
57. Hasan, M.F.; Abuel-Naga, H. Effect of Temperature and Water Salinity on Electrical Surface Conduction of Clay Particles. *Minerals* **2023**, *13*, 1110. [CrossRef]
58. Costa Reis, M. Ion Activity Models: The Debye-Hückel Equation and Its Extensions. *ChemTexts* **2021**, *7*, 9. [CrossRef]
59. Blossey, R. The Poisson–Boltzmann Equation. In *The Poisson–Boltzmann Equation: An Introduction*; Blossey, R., Ed.; Springer International Publishing: Cham, Switzerland, 2023; pp. 1–25. ISBN 978-3-031-24782-8.
60. Rice, C.L.; Whitehead, R. Electrokinetic Flow in a Narrow Cylindrical Capillary. *J. Phys. Chem.* **1965**, *69*, 4017–4024. [CrossRef]
61. Kim, S.I.; Kim, S.J. Analysis of the Electroviscous Effects on Pressure-Driven Flow in Nanochannels Using Effective Ionic Concentrations. *Microfluid. Nanofluid.* **2017**, *22*, 12. [CrossRef]
62. Murrell, J.N. Avogadro and His Constant. *Helv. Chim. Acta* **2001**, *84*, 1314–1327. [CrossRef]
63. Zhang, P. *Physical Chemistry*, 2nd ed.; Chemical Industry Press Co., Ltd.: Beijing, China, 2023; ISBN 978-7-122-42316-0.
64. Gould, W.J.; Cunningham, S.A. Global-Scale Patterns of Observed Sea Surface Salinity Intensified since the 1870s. *Commun. Earth Environ.* **2021**, *2*, 1–7. [CrossRef]
65. Iversen, N.; Jørgensen, B.B. Diffusion Coefficients of Sulfate and Methane in Marine Sediments: Influence of Porosity. *Geochim. Cosmochim. Acta* **1993**, *57*, 571–578. [CrossRef]
66. Lin, L.I.-K. A Concordance Correlation Coefficient to Evaluate Reproducibility. *Biometrics* **1989**, *45*, 255–268. [CrossRef]
67. Lin, L.; Hedayat, A.S.; Wu, W. *Statistical Tools for Measuring Agreement*; Springer: New York, NY, USA, 2012; ISBN 978-1-4614-0561-0.
68. Zaffar, M.; Lu, S.-G. Pore Size Distribution of Clayey Soils and Its Correlation with Soil Organic Matter. *Pedosphere* **2015**, *25*, 240–249. [CrossRef]

69. Kuila, U.; Prasad, M. Specific Surface Area and Pore-Size Distribution in Clays and Shales. *Geophys. Prospect.* **2013**, *61*, 341–362. [CrossRef]

70. Cheng, Q.; Ng, C.W.W.; Zhou, C.; Tang, C.S. A New Water Retention Model That Considers Pore Non-Uniformity and Evolution of Pore Size Distribution. *Bull. Eng. Geol. Environ.* **2019**, *78*, 5055–5065. [CrossRef]

71. Zhou, C.; Ng, C.W.W. A New and Simple Stress-Dependent Water Retention Model for Unsaturated Soil. *Comput. Geotech.* **2014**, *62*, 216–222. [CrossRef]